Viscoelastic instability in an asymmetric geometry

Manish Kumar¹ and Arezoo M. Ardekani¹

¹Department of Mechanical Engineering, Purdue University, 585 Purdue Mall, West Lafayette, Indiana 47907 USA

Viscoelastic flow through porous media is important in industrial applications such as enhanced oil recovery (EOR), microbial mining, and groundwater remediation. It is also relevant in biological processes such as drug delivery, infectious biofilm formation, and transport during respiration and fertilization. The porous medium is highly disordered and viscoelastic instability-induced flow states at the pore-scale regulate the transport in porous media. In the present study, we systematically explore the effect of geometrical asymmetry on pore-scale viscoelastic instability. The asymmetric geometry used in the present study consists of two cylinders confined inside a channel, where the front cylinder is located on the centerline of the channel and the rear cylinder is situated off-center of the channel. The geometrical asymmetry facilitates asymmetric flow around both cylinders. An eddy also appears in the region between the cylinders at intermediate Weissenberg numbers, where the Weissenberg number characterizes the relative importance of elastic and viscous forces in viscoelastic flows. We further explore the effect of the strength of geometrical asymmetry and fluid rheological properties on flow asymmetry and eddy formation.

I. INTRODUCTION

Interaction between curved-geometry and the polymeric solution often induces viscoelastic instability due to the stretching of the polymeric chains along the curvature [1, 2]. Porous media are made of randomly shaped grains and have inbuilt curved surfaces [3, 4]. The flow of polymeric solutions through porous media is important in several industrial and natural applications [5]. Polymeric solutions are injected through porous rocks to mobilize capillary trapped immiscible fluids during industrial applications such as enhanced oil recovery [6] and groundwater remediation [7]. The stretching of polymeric chains induces large elastic stresses [8], leading to elastic instability at Weissenbergs number (Wi) greater than a crit-

ical value [9–11]. The Weissenberg number represents the ratio of elastic to viscous forces [12]. Elastic instability can lead to time-depend chaotic flow even at the negligible inertia, which is also known as "elastic turbulence" due to its analogous feature to inertial turbulence [13, 14]. The spatiotemporal flow fluctuations resulting from elastic turbulence [15–18] facilitate unpinning and mobilization of trapped fluid ganglia [19, 20]. The flow of polymeric solutions through porous media is also relevant in many natural processes, including the transport of biofilms and biological fluids [5, 21]. The flow of biological fluids through poroelastic tissues plays a critical role in targeted drug delivery [22] and bacterial infection [23].

The study of pore-scale viscoelastic instability is essential to understand the sample-scale transport of fluids and particles in viscoelastic porous media flow [4]. Viscoelastic flow around a cylinder confined in a channel is the simplest model used to investigate pore-scale instability around the obstacle present in porous media [24–26]. The flow state induced by the viscoelastic instability for a cylinder confined in a channel depends on the blockage ratio. Viscoelastic flow induces a long elastic wake downstream of the cylinder [24, 27]. At a small blockage ratio (< 0.5), the elastic wake loses the lateral symmetry for Wi > Wi_{cr} in shear-thinning viscoelastic fluids, leading to an asymmetric flow around the cylinder [25, 27, 28]. Whereas viscoelastic instability induces unstable eddy upstream of the cylinder at a high blockage ratio [26, 29, 30]. The polymeric chains advect faster than they relax for densely placed obstacles in the porous media. Therefore, the polymeric chains do not have sufficient time to relax before reaching the next obstacle. The channels consisting of multiple cylinders in streamwise direction have been used to investigate the hydrodynamic interaction between successive obstacles [10, 31, 32]. Viscoelastic flow through a channel having a pair of streamwise located cylinders undergoes two successive transitions due to elastic instability, leading to the formation of three different flow states in the region between the cylinders [10]. Corrugated channels also have been used to explore the viscoelastic interaction between successive pores of a porous media, where multiple stochastically switching flow states have been reported inside the pores of the channel [9, 33].

The investigations of pore-scale viscoelastic instabilities have been mainly focused on symmetric geometries [9, 10, 25, 34–39]. However, the natural and engineered porous media are highly complex and disordered [3, 4, 40, 41]. Therefore, the criteria and the dynamics of elastic instabilities obtained in the simple symmetric geometries fail to explain the sample-

scale elastic instability in 2D and 3D porous geometries [11, 15, 16]. We investigate porescale viscoelastic instability in an asymmetric geometry in the present study. We show that introducing even the slightest asymmetry in the geometry leads to a major impact on the criterion of viscoelastic instability and the flow state resulting from the instability. We investigate the impact of the emergence of distinct flow states on transport in an asymmetric geometry. We also quantify the polymeric stress field and find that the topology of the polymeric stress field regulates the existence of distinct flow states and hence controls fluid transport.

II. GEOMETRY AND GOVERNING EQUATIONS

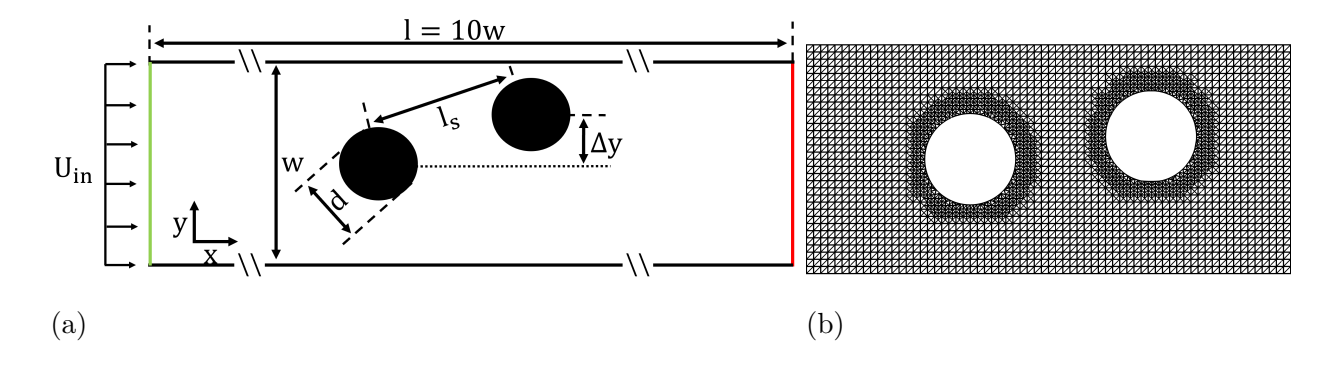


FIG. 1: (a) The schematic of simulation geometry. The front cylinder is located on the centerline of the channel, whereas the rear cylinder is off the centerline and Δy represents its deviation from the centerline. The diameter of the cylinders is $d=160~\mu\mathrm{m}$ and $l_s=2d$ is the separation between the cylinders. The channel length ($l=4~\mathrm{mm}$) is much larger than the width ($w=0.4~\mathrm{mm}$) and cylinder diameter ($d=160~\mu\mathrm{m}$). The inlet and the exit of the channel are located at x/d=-9.4 and x/d=15.6, respectively. The front cylinder is located at x=0, which ensures that the entrance and exit effects are negligible (see Appendix VIA). Black solid lines represent solid boundaries, whereas green and red lines indicate the inlet and exit of the channel, respectively. (b) A cartoon showing a coarse numerical mesh (320×32) close to the cylinders. The simulations have been performed using a finer mesh (2560×256).

To investigate the effect of geometrical asymmetry on pore-scale viscoelastic instability, we consider a geometry that has two cylinders located inside a channel (Fig. 1a). The

front cylinder is on the centerline of the channel, whereas the rear cylinder is located off the centerline. The deviation of the rear cylinder from the centerline (Δy) quantifies the strength of asymmetry, where the geometry becomes symmetric in the limit of $\Delta y \to 0$. We change Δy in the present study and explore how the strength of geometrical asymmetry affects viscoelastic instability.

The governing equations based on the conservation of mass and momentum for an incompressible polymeric fluid of density ρ can be given as:

$$\nabla \cdot \mathbf{u} = 0, \tag{1}$$

$$\rho \left(\frac{\partial \mathbf{u}}{\partial t} + \mathbf{u} \cdot \nabla \mathbf{u} \right) = -\nabla p + \nabla \cdot (\boldsymbol{\tau}_s + \boldsymbol{\tau}_p), \tag{2}$$

where \mathbf{u} and p are the velocity and pressure fields, respectively. The contribution of Newtonian solvent to the stress is calculated as $\boldsymbol{\tau}_s = \eta_s(\nabla \mathbf{u} + \nabla \mathbf{u}^T)$, where η_s is the solvent viscosity. The contribution of polymeric chains to the stress tensor is represented by $\boldsymbol{\tau}_p$. The FENE-P constitutive model has been used to obtain the polymeric stress tensor $(\boldsymbol{\tau}_p)$ [42–44]. This model considers the finite stretching of the polymeric chains and also captures both elastic and shear-thinning behaviors of the polymeric solution. The FENE-P constitutive equation for a polymeric solution of relaxation time λ can be described as:

$$\boldsymbol{\tau}_p + \frac{\lambda \nabla}{f} \boldsymbol{\tau}_p = \frac{a\eta_p}{f} (\nabla \mathbf{u} + \nabla \mathbf{u}^T) - \frac{D}{Dt} \left(\frac{1}{f} \right) [\lambda \boldsymbol{\tau}_p + a\eta_p \mathbf{I}], \tag{3}$$

where η_p denotes the polymeric contribution to the zero-shear rate viscosity of the solution. The material derivative is calculated as $\frac{D}{Dt} = \frac{\partial}{\partial t} + \mathbf{u} \cdot \nabla$ and $\overset{\nabla}{\boldsymbol{\tau}}_p = \frac{D\boldsymbol{\tau}_p}{Dt} - \boldsymbol{\tau}_p \cdot \nabla \mathbf{u} - \nabla \mathbf{u}^T \cdot \boldsymbol{\tau}_p$ represents the upper convective time derivative of $\boldsymbol{\tau}_p$. The identity tensor is denoted by \mathbf{I} and $a = L^2/(L^2 - 3)$, where L^2 characterizes the maximum stretching of the polymeric chains [42, 45, 46]. The nonlinear function $f(\boldsymbol{\tau}_p)$ for the FENE-P model can be written as:

$$f(\tau_p) = \frac{L^2 + \frac{\lambda}{a\eta_p} tr(\tau_p)}{L^2 - 3},\tag{4}$$

where $tr(\tau_p)$ represents the trace of polymeric stress tensor. The trace of polymeric stress tensor is the sum of the elements on the main diagonal and represents the stress due to the stretching of the polymeric chains in viscoelastic flows.

The numerical simulations have been performed using OpenFOAM, which is an open-source numerical tool based on finite volume method [47]. Further, we integrate a viscoelastic

solver named RheoTool [48] with OpenFOAM to compute the polymeric stress tensor. The log-conformation approach has been used to calculate the polymeric stress tensor [48, 49]. This method linearizes the exponential profile of polymeric stress tensor in the regions of high deformation rate and ensures the positive definiteness of the stress tensor, which enables to perform the numerical simulations at high Weissenberg numbers [50–52]. In the log-conformation method, the governing equations of polymeric stress tensor are solved for the logarithm of conformation tensor (Θ) , and the following relation is used to obtain the polymeric stress tensor (τ_p) from the log-conformation tensor (Θ) :

$$\tau_p = \frac{\eta_p}{\lambda} (f e^{\Theta} - a \mathbf{I}). \tag{5}$$

The governing equations have been discretized based on the finite volume method. Gauss's theorem has been used to calculate the divergence. The Gaussian deferred correction component-wise schemes (GaussDefCmpw) have been used to discretize the convective terms in the governing equations, where the "CUBISTA" scheme has been used for the convective terms in the viscoelastic equation. The Gauss gradient scheme with linear interpolation (Gauss linear) has been used to calculate cell gradient. The Laplacian operator can be represented using the combination of the divergence and gradient operators. Therefore, the scheme based on the Gauss theorem has been also used to discretize the Laplacian terms. For temporal evolution, the Crank-Nicolson method has been used. The validation of the numerical tool and the details of numerical methodology have been discussed in the literature [48, 49]. Furthermore, the applicability of the present tool to investigate viscoelastic flows is evident from our recent publications [9, 10]. The computational domain has been discretized using 2560×256 static grid points and the five layers close to the cylinders have been further refined (Fig. 1b). The time-step in the simulation has been controlled by the Courant number (Co). In the present study, we use $Co_{max} = 0.025$. The details of mesh and time-step dependence studies have been given in Appendix VIB. The simulations have been performed for dimensionless time t=20, where λ has been used to normalize the time. The simulation achieves a steady-state or the instability becomes fully developed for dimensionless time t > 5 (Appendix VIB). The simulation time (t = 20) is sufficient for the convergence of the statistics.

The Weissenberg number is the most important dimensionless number in the present study and it has been defined as Wi= $\lambda U_{in}/d$, where U_{in} is the inlet flow velocity. The

TABLE I: The range of different parameters used in the study.

ρ	λ	U_{in}	β	L^2
1000 kg/m^3	1 s	0.1 - 0.6 mm/s	0.05 - 0.2	100-1000

value of Wi in the present study ranges in Wi = 0-4. The effect of inertia is negligible as the Reynolds number (Re= $\rho U_{in} d/\eta_0$), which represents the ratio of inertial to viscous forces, is very small (Re < 0.005). The zero-shear rate viscosity of the polymeric solution is shown as $\eta_0 = \eta_s + \eta_p$. We define $\beta = \eta_s/\eta_0$ as the viscosity ratio, which represents the strength of shear-thinning in the FENE-P model. The density of the polymeric solution commonly used in the experiment is close to the water, whereas the value of the viscosity ratio lies in the range of $\beta = 0.05 - 0.25$ [11, 27]. The relaxation time of the polymeric solution has been reported in the range of $\lambda = 0.1 - 10 \ s$ [11, 27, 34, 53]. For the FENE-P model, a typical value of L^2 found in the literature for polymeric solution is in the range of $L^2 = 10 - 1000$ [42, 46, 54, 55]. The values of inlet velocity and fluid rheological parameters used in the present study have been summarized in Table I. The response of the FENE-P model in the homogeneous shear and extensional flows for the different combinations of the parameters have been shown in Fig. 2a and Fig. 2b, respectively [56]. The viscosity ratio (β) has the dominant effect on the shear viscosity. Whereas, L^2 has the dominant effect on the extensional viscosity. Throughout the study, inlet velocity (U_{in}) and characteristic shear stress $(\eta_0 U_{in}/d)$ have been used to normalize the velocity field and the stress field, respectively. We also use $\eta_0 U_{in}/d$ to normalize the pressure.

III. RESULTS AND DISCUSSION

In our recent publication, we have investigated viscoelastic instability in the symmetric geometry, where both the cylinders in the channel are located on the centerline (i.e., $\Delta y = 0$) [10]. Viscoelastic instability induces three distinct flow states in the region between the cylinder in the symmetric geometry. These flow states are characterized by the flow symmetry around the cylinders and the existence of eddy between the cylinders [10]. The symmetric flow state is eddy-free for Wi < Wi_{cr1} (flow state type-1), whereas the eddies appear in the region between the cylinders for Wi_{cr1} < Wi < Wi_{cr2} (type-2). The flow around the cylinders

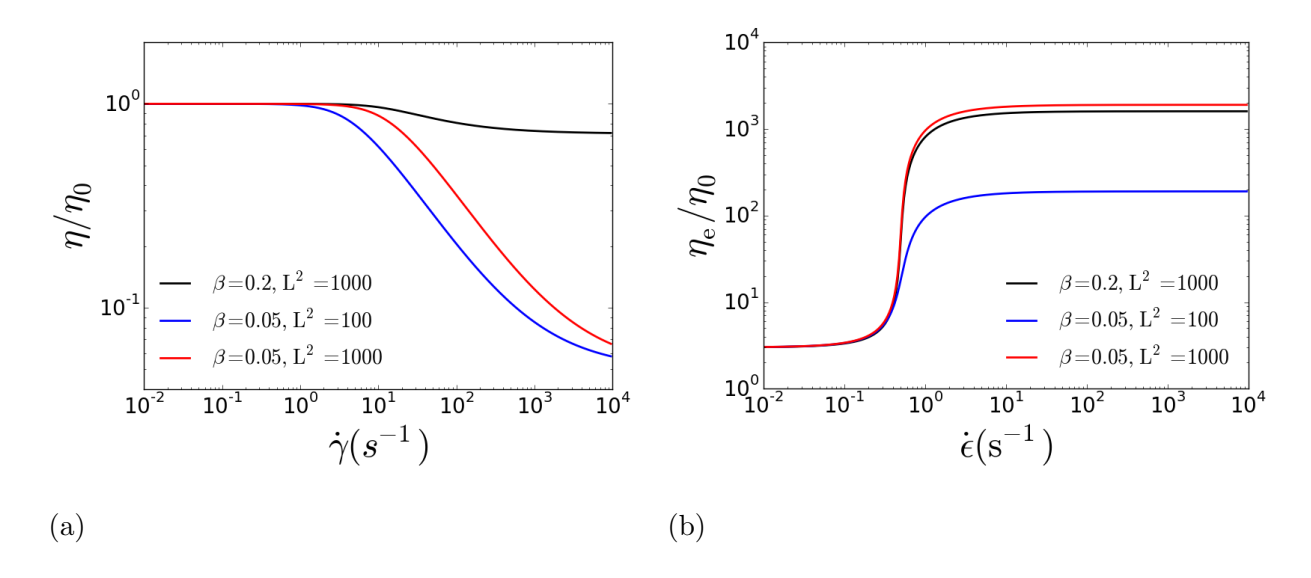


FIG. 2: (a) Shear viscosity (η) and (b) extensional viscosity (η_e) prediction of FENE-P model for different combinations of the parameters.

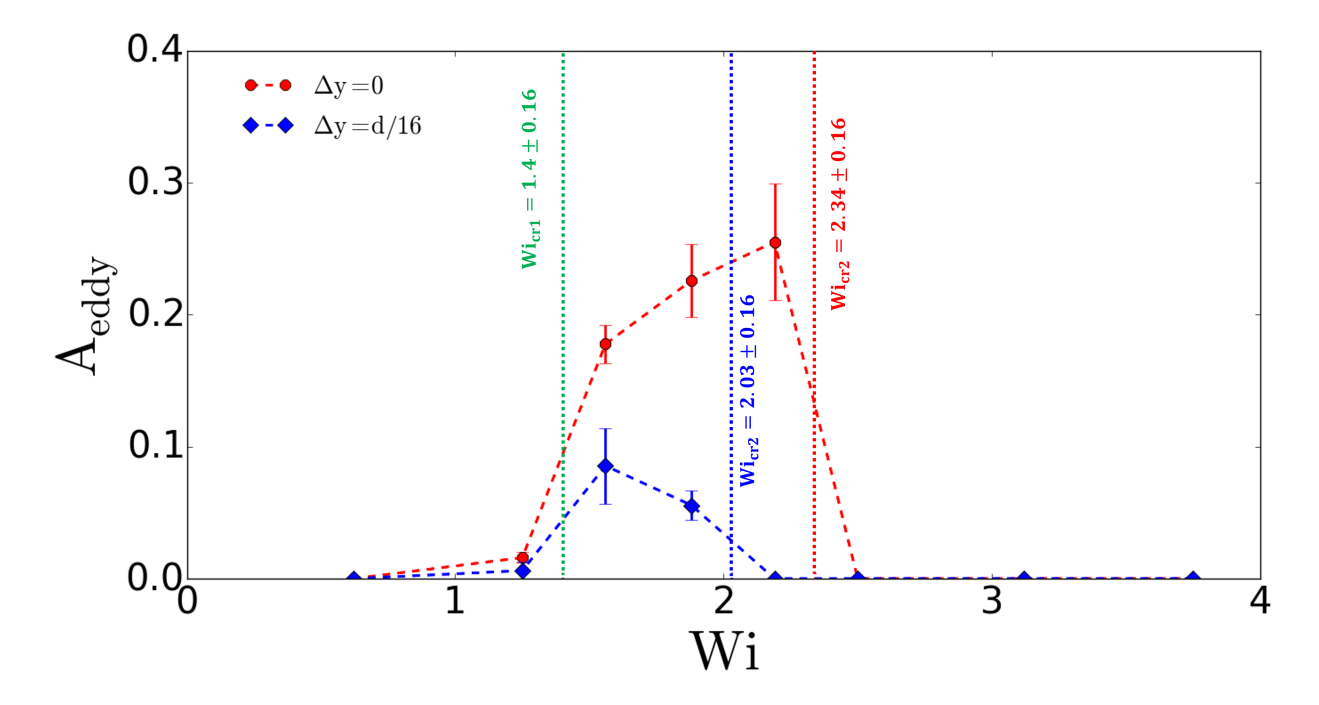


FIG. 3: The area occupied by eddies in the region between the cylinders (A_{eddy}) for a symmetric geometry $(\Delta y = 0)$ and an asymmetric geometry $(\Delta y = d/16)$. A_{eddy} has been normalized by $l_s d$. The symbols and the error-bars represent the mean value and the standard-deviation, respectively. Other parameters are $\beta = 0.05$ and $L^2 = 1000$.

becomes asymmetric with the loss of eddy for $Wi > Wi_{cr2}$ (type-3). Fig. 3 depicts the area

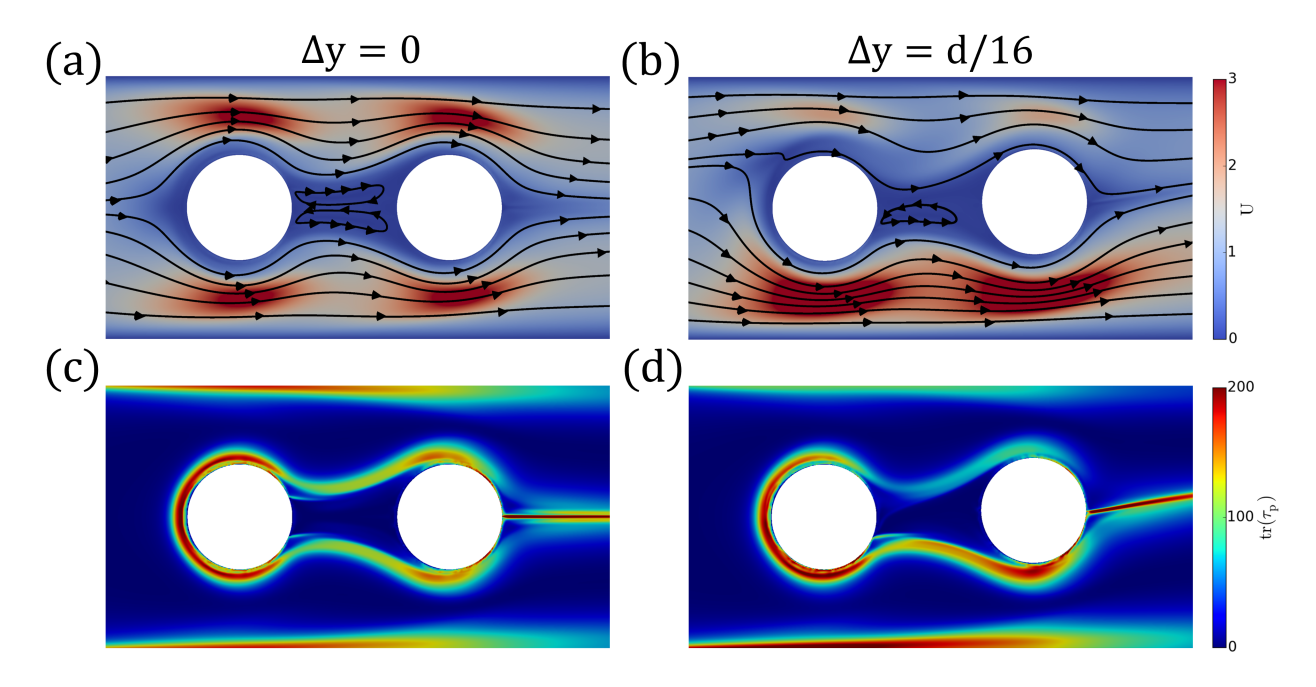


FIG. 4: (a,b) Velocity field and (c,d) the trace of polymeric stress tensor at Wi = 1.56 for (a,c) a symmetric geometry ($\Delta y = 0$) and (b,d) an asymmetric geometry ($\Delta y = d/16$). Other parameters are $\beta = 0.05$, $L^2 = 1000$, and t = 17.5.

occupied by eddies (A_{eddy}) in symmetric $(\Delta y = 0)$ and asymmetric geometries $(\Delta y = d/16)$. Even in the asymmetric geometry, the formation of eddy occurs between the cylinders for $\mathrm{Wi_{cr1}} < \mathrm{Wi} < \mathrm{Wi_{cr2}}, \ \mathrm{and} \ \mathrm{the} \ \mathrm{geometry} \ \mathrm{become} \ \mathrm{eddy} \ \mathrm{free} \ \mathrm{for} \ \mathrm{Wi} < \mathrm{Wi_{cr1}} \ \mathrm{and} \ \mathrm{Wi} > \mathrm{Wi_{cr2}}.$ The minimum Wi (Wi_{cr1}) required for the formation of the eddy is similar for both geometries. However, the critical Wi required for the second transition (Wi_{cr2}) is larger in the symmetric geometry. Therefore, the eddy between the cylinders exists up to a higher Wi in the symmetric geometry compared to the asymmetric geometry (Fig. 3). Furthermore, the area occupied by the eddy in the symmetric geometry ($\Delta y = 0$) is much larger than the asymmetric geometry ($\Delta y = d/16$). Fig. 4 depicts the flow field and the trace of polymeric stress tensor for the symmetric and asymmetric geometries at a Weissenberg number where both of the geometries have eddies. In the symmetric geometry, the flow around the cylinders remain symmetric and a pair of recirculating eddies appear in the region between the cylinders (Fig. 4a), whereas the flow is asymmetric and only one eddy appears in between the cylinders for the asymmetric geometry (Fig. 4b). Therefore, A_{eddy} in the asymmetric geometry is smaller than the symmetric geometry. The topology of the polymeric stress field controls the flow state in viscoelastic flows [9, 10]. The streak characterized by large polymeric stresses forms in a viscoelastic flow, which leads to flow separation and formation of distinct flow states. The elastic wake in between the cylinders bifurcates and forms symmetric topology in the symmetric geometry (Fig. 4c), which induces the formation of two eddies in the region encircled by the streaks of high polymeric stress (Fig. 4a). Even in the asymmetric geometry, the elastic wake has two branches between the cylinders (Fig. 4d). However, it does not form the symmetric topology as the value of stress in the lower branch is much larger than the top branch. Therefore, it leads to the formation of an asymmetric flow state and induces only one eddy in between the cylinders (Fig. 4b). It has been shown that the location of the maximum value of Pakdel–McKinley (M) parameter [2, 38] denotes the most sensitive region for elastic instability and hence it can be used to predict the flow state after the instability [10]. Similar to the symmetric geometry ($\Delta y = 0$), even in the asymmetric geometry ($\Delta y = d/16$), the location of M_{max} shifts from the side of the rear cylinder to the region in between the cylinders as $Wi \to Wi_{cr1}$ (Appendix VI D). Therefore, the formation of a new flow state in the asymmetric geometry ($\Delta y = d/16$) at $Wi_{cr1} < Wi < Wi_{cr2}$ occurs due to the instability in the region between the cylinders.

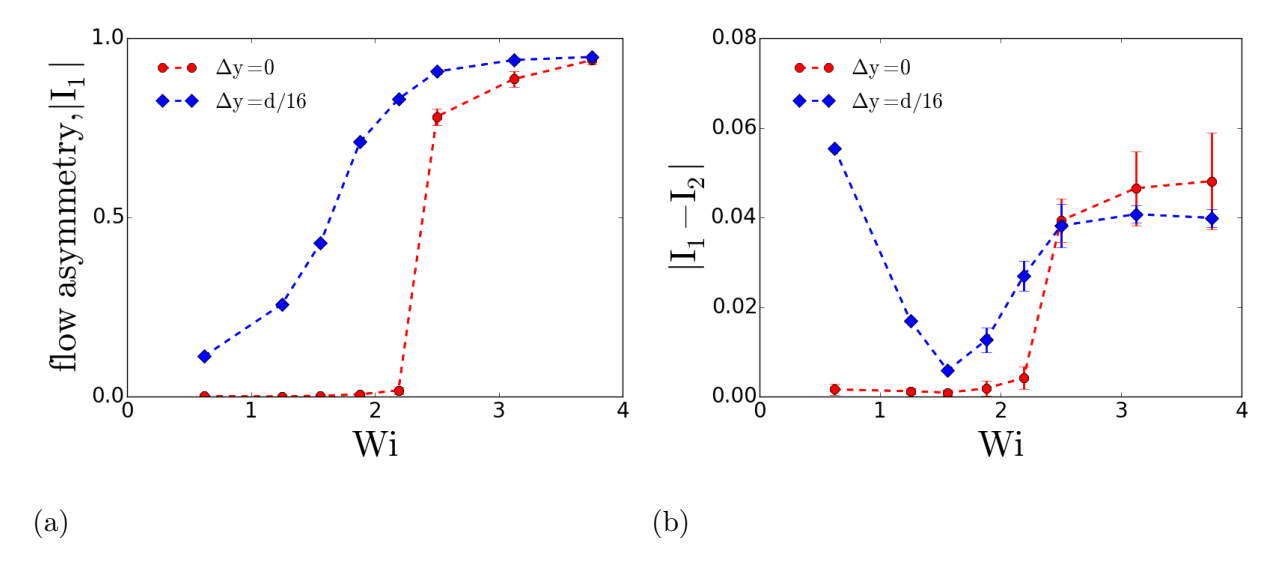


FIG. 5: (a) Flow asymmetry around the front cylinder (I_1) and (b) the difference between the flow asymmetries around the front and rear cylinders $(I_1 - I_2)$ at different Wi for both the symmetric $(\Delta y = 0)$ and asymmetric $(\Delta y = d/16)$ geometries. The symbols and the error-bars represent the mean value and the standard-deviation, respectively. Other parameters are $\beta = 0.05$ and $L^2 = 1000$.

To quantify the flow asymmetry around the cylinders, we define an asymmetry parameter

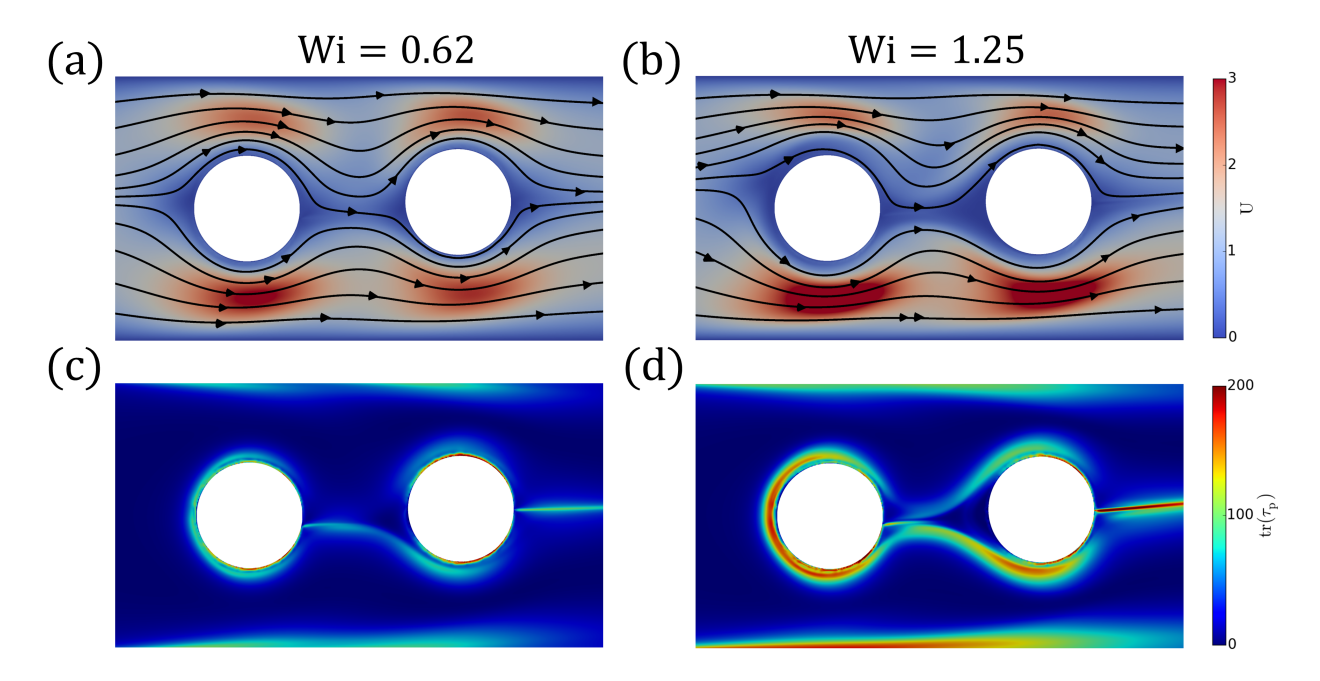


FIG. 6: (a,b) Velocity field and (c,d) the trace of polymeric stress tensor in the asymmetric geometry ($\Delta y = d/16$) at (a,c) Wi = 0.62 and (b,d) Wi = 1.25. Streamline changes lane in between the cylinders at Wi = 0.62. Other parameters are $\beta = 0.05$, $L^2 = 1000$, and t = 17.5 (steady state).

I as:

$$I = \frac{Q_{upper} - Q_{lower}}{Q_{upper} + Q_{lower}},\tag{6}$$

where Q_{upper} and Q_{lower} represent the volumetric flow rate through the upper and lower gap of the channel at the location of the cylinder. I_1 and I_2 represent the flow asymmetry around the front cylinder and the rear cylinder of the channel, respectively. The value of flow asymmetry (I) fluctuates around a well-defined mean once the instability becomes fully developed (Appendix VIC). However, the standard deviation of the fluctuation is very small (< 1% of the mean value) indicating an almost steady flow even at Wi > Wi_{cr2}. In the symmetric geometry, the flow around the cylinders remains symmetric $(I_1 = 0)$ until the second transition occurs (Wi < Wi_{cr2}) and after that (i.e., Wi > Wi_{cr2}) I_1 rapidly increases with Wi (Fig. 5a). Whereas, the flow around the cylinders is always asymmetric $(I_1 > 0)$ in the asymmetric geometry and it gradually increases with Wi before it saturates, unlike the sharp change of I_1 in the symmetric geometry (Fig. 5a). We recall that the front cylinder is located on the centerline of the channel even in the asymmetric geometry. However, the flow around it is asymmetric even at small Wi due to the hydrodynamic

interaction between the front and the rear cylinders. The values of flow asymmetry around the front (I_1) and the rear (I_2) cylinders are not identical for asymmetric flow states [10]. Therefore, there is a net spanwise transport of fluid in the region between cylinders. We calculate the difference between the flow asymmetry around the front and rear cylinders $(I_1 - I_2)$ to quantify the spanwise transport of fluid between the cylinders (Fig. 5b). In the symmetric geometry, $I_1 - I_2 \approx 0$ for Wi < Wi_{cr2} and it increases rapidly once the flow state becomes asymmetric. Whereas, the value of $I_1 - I_2$ exhibits a non-monotonic trend with Wi in the asymmetric geometry (Fig. 5b). Initially, the value of $I_1 - I_2$ decreases with Wi, obtains a minimum value, and then increases as Wi further increases. To explain this non-monotonic trend of $I_1 - I_2$ in the asymmetric geometry, we plot streamlines and stress field at a small Wi (Wi = 0.62) and an intermediate Wi (Wi = 1.25) in Fig. 6. Due to geometrical asymmetry, there is a spanwise transport of fluid between the cylinders even at a small Wi, where the viscoelastic effect is negligible (Fig. 6a). As Wi increases, streaks of high polymeric stress form, connecting the cylinders (Fig. 6d) and resisting the spanwise transport of fluid at intermediate Wi (Fig. 6b). Ultimately, the flow around the cylinders becomes completely asymmetric $(I_1 \approx 1)$ at large Wi (Fig. 5a), leading to the enhancement of spanwise transport of fluid between the cylinders (Fig. 5b). The influence of the rear cylinder on the front cylinder weakens as the separation between the cylinders (l_s) increases. Therefore, the formation of the eddy between the cylinders does not occur and the value of I_1 is smaller in the geometry having a larger separation (i.e., $l_s = 3d$) between the cylinders (Fig. 7a). However, a larger separation between the cylinders $(l_s = 3d)$ facilitates spanwise transport in the asymmetric geometry. Therefore, the value of $I_1 - I_2$ is higher for the geometry with a larger separation between the cylinders (Fig. 7b).

To explore the instability downstream of the rear cylinder, we plot flow asymmetry (I) inside the channel in symmetric and asymmetric geometries as a function of downstream position at different Wi (Figs. 8a and 8b). The flow asymmetry decays downstream of the rear cylinder and ultimately (x/d > 8) the flow inside the channel becomes symmetric (I = 0). In the symmetric geometry $(\Delta y = 0)$, the second transition (Wi_{cr2}) occurs at a larger Wi compared to the asymmetric geometry $(\Delta y = d/16)$ (Fig. 3). Therefore, the value of flow asymmetry around the cylinder does not saturate in the symmetric geometry at Wi = 2.5 (Fig. 5a), which leads to a smaller value of I in the symmetric geometry compared to the value in the asymmetric geometry at the location of the rear cylinder

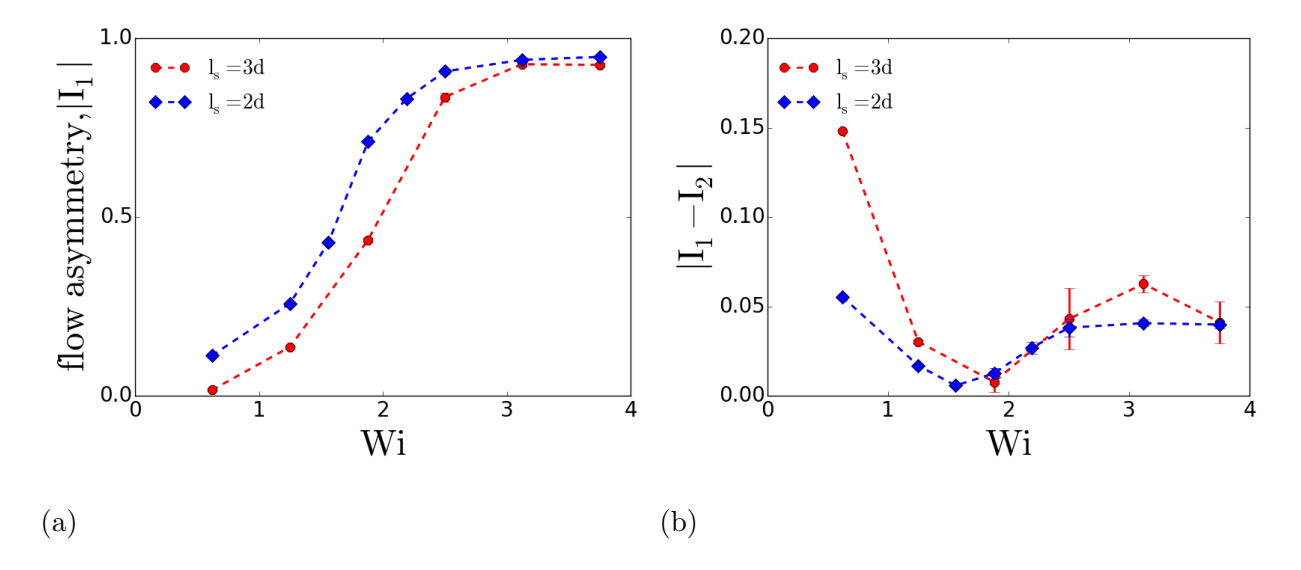


FIG. 7: (a) I_1 and (b) $I_1 - I_2$ at different Wi in the asymmetric ($\Delta y = d/16$) geometries having different separation between the cylinders (l_s). Other parameters are $\beta = 0.05$ and $L^2 = 1000$.

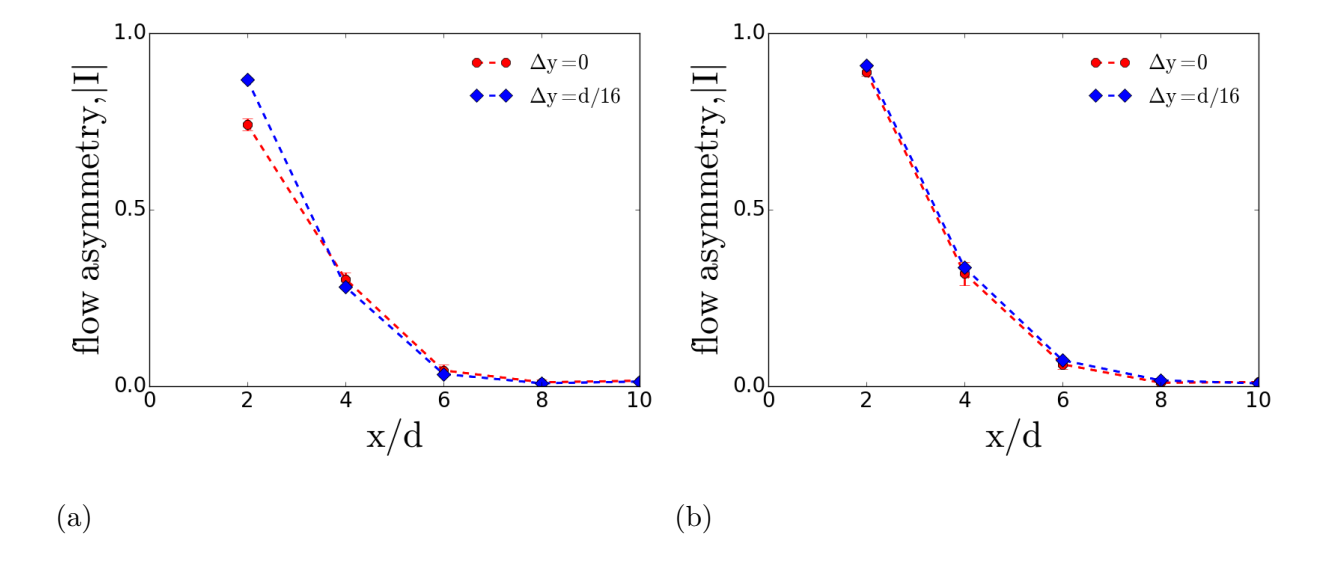


FIG. 8: Flow asymmetry (I) downstream of the rear cylinder for symmetric ($\Delta y = 0$) and asymmetric ($\Delta y = d/16$) geometries at (a) Wi = 2.5 and (b) Wi = 3.75. x/d = 0 is the location of the center of the front cylinder. Other parameters are $\beta = 0.05$ and $L^2 = 1000$.

(Fig. 8a). However, the locations downstream of the rear cylinder, I have similar values for different geometries (Fig. 8a). At large Wi (Wi = 3.75), the value of flow asymmetry around the cylinder saturates and both the geometries have similar values. Therefore, there is no significant difference between the values of I of symmetric and asymmetric geometries

at the locations downstream of the rear cylinder (Fig. 8b). As Wi increases, the cylinder wake influences larger distances downstream of the cylinder. Therefore, the decay rate of I slightly decreases as Wi increases (Figs. 8a and 8b).

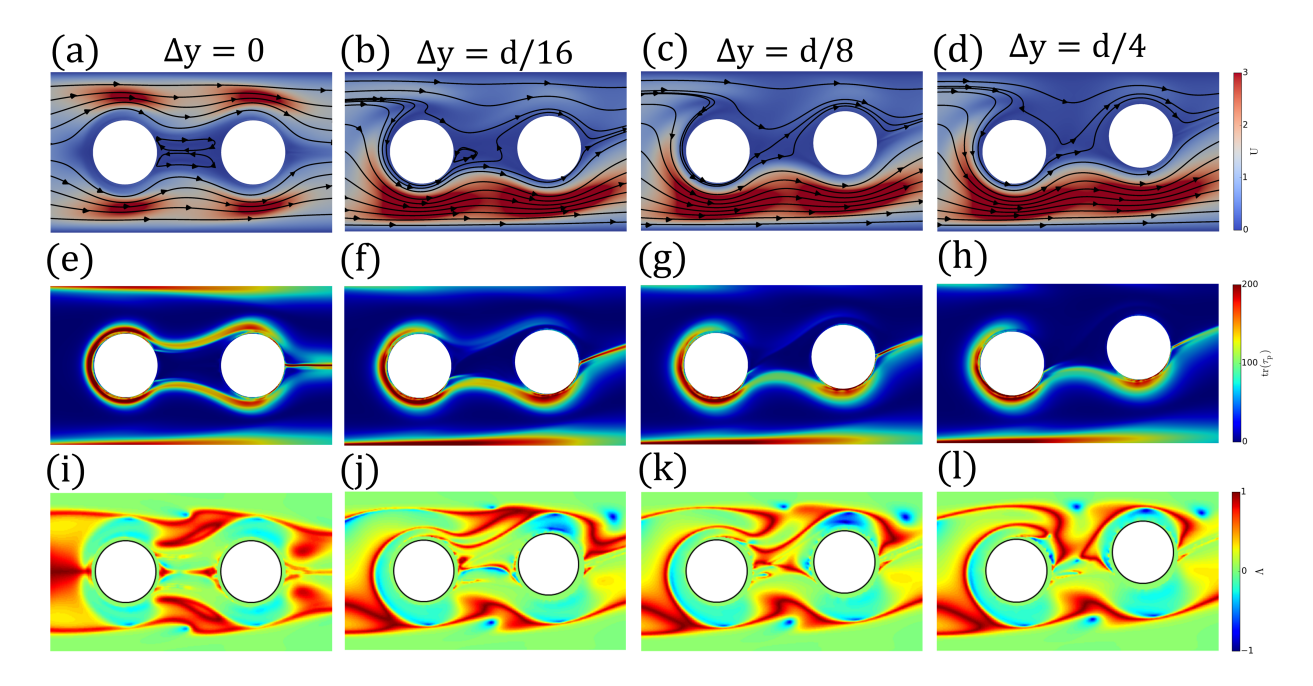


FIG. 9: (a-d) Velocity field, (e-h) the trace of polymeric stress tensor, and (i-l) flow-type parameter (Λ) at Wi = 1.88 in the geometries having (a,e,i) $\Delta y = 0$, (b,f,j) $\Delta y = d/16$, (c,g,k) $\Delta y = d/8$, and (d,h,l) $\Delta y = d/4$. Other parameters are $\beta = 0.05$, $L^2 = 1000$, and t = 17.5.

The flow states for the different strengths of geometrical asymmetry (Δy) have been shown in Fig. 9(a-d). The number of eddies in the region between the cylinders decreases from two in the symmetric geometry (Fig. 9(a)) to one in the asymmetric geometry (Fig. 9(b)). Further, in the asymmetric geometries, the size of the eddy also decreases as the strength of geometrical asymmetry (Δy) increases, and ultimately the eddy completely disappears in highly asymmetric geometries $(\Delta y > d/8)$. As the strength of geometrical asymmetry increases, either branch of the elastic wake (top branch in Fig. 9 (e-h)) weakens and ultimately disappears, which induces the loss of eddy and the formation of the eddy-free flow state. The flow-type parameter (Λ) is a metric to characterize the local fluid deformation in mixed flows. It can be defined as: $\Lambda = (|\mathbf{D}| - |\Omega|)/(|\mathbf{D}| + |\Omega|)$, where $|\mathbf{D}|$ and $|\Omega|$ are the magnitudes of strain rate tensor and vorticity tensor, respectively [5]. The value of Λ varies from $\Lambda = -1$ for purely rotational flow to $\Lambda = 0$ for purely shear flow to $\Lambda = 1$

for purely extensional flow. The streaks of large polymeric stress act as barriers and resist the flow crossing the region of high stress. Therefore, the regions where the streaks of high polymeric stress form are shear-dominated (Fig. 9 (i-l)).

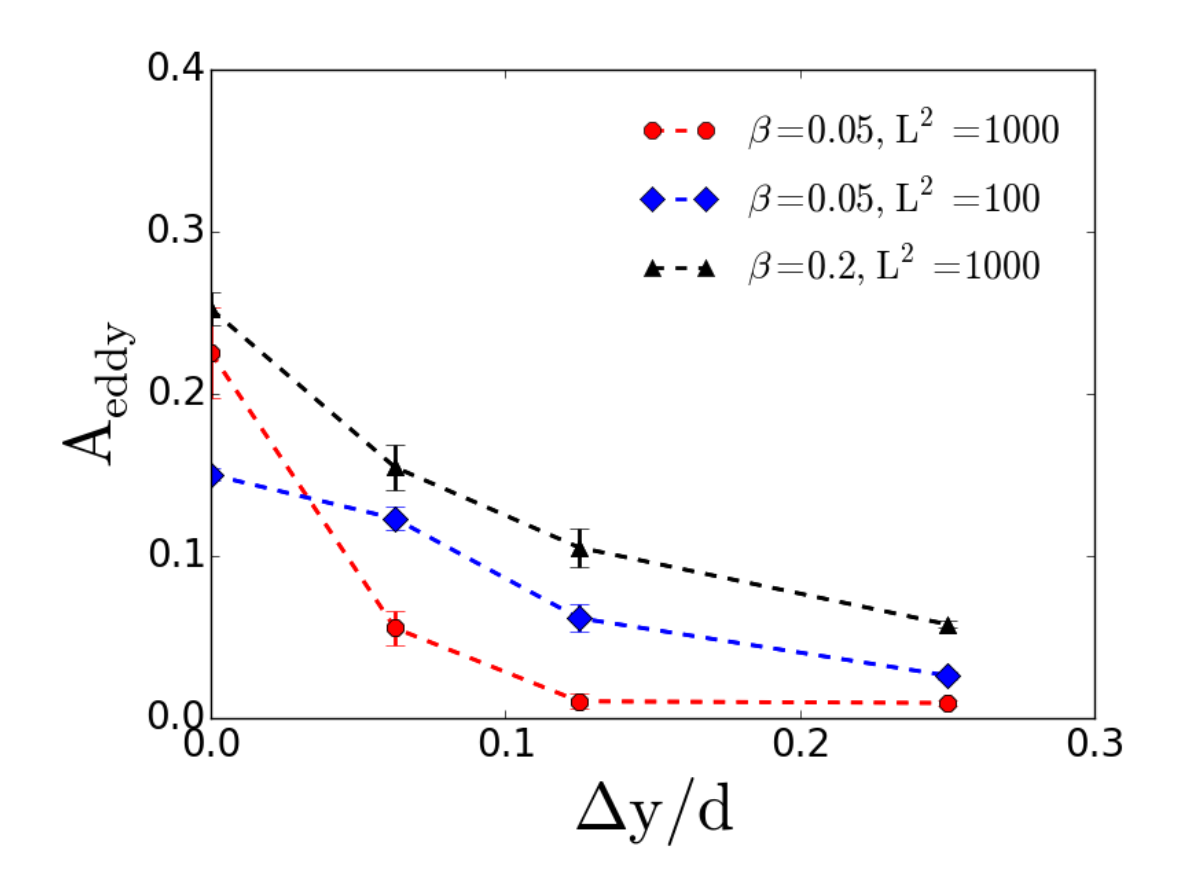


FIG. 10: The area occupied by eddy (A_{eddy}) at Wi = 1.88 for the geometries of different strength of asymmetry (Δy) and different rheological properties.

We quantify the area occupied by eddy (A_{eddy}) for the different values of geometrical asymmetry (Δy) and fluid rheological parameters $(\beta \text{ and } L)$ in Fig. 10. The value of A_{eddy} decreases monotonically as Δy increases due to the loss of eddy for the transition from symmetric $(\Delta y = 0)$ to asymmetric $(\Delta y = d/16)$ geometry and then due to the shrinkage of eddy size as Δy further increases (Fig. 10). A weakly shear-thinning fluid stabilizes the eddy between the cylinders [10] and the strength of shear-thinning decreases as the solvent's contribution to the total viscosity of the polymeric solution (β) increases. Therefore, A_{eddy} increases as the viscosity ratio of the solution (β) increases (Fig. 10). This facilitates the existence of eddy between the cylinders up to a larger value of Δy as the viscosity ratio (β) increases. The elastic property of the solution decreases as the maximum extensibility

of the polymeric chains (L^2) decreases. Hence, A_{eddy} for the symmetric geometry decreases as L^2 decreases (Fig. 10). The elasticity of the fluid also has a destabilizing effect on the eddy between the cylinders [10]. Therefore, A_{eddy} for the asymmetric geometries increases as the value of L^2 decreases (Fig. 10). Due to the destabilizing effect of shear-thinning and elasticity of the fluid, the flow becomes eddy-free at a much smaller Δy for the strongly shear-thinning and strong elastic fluid (Fig. 10).

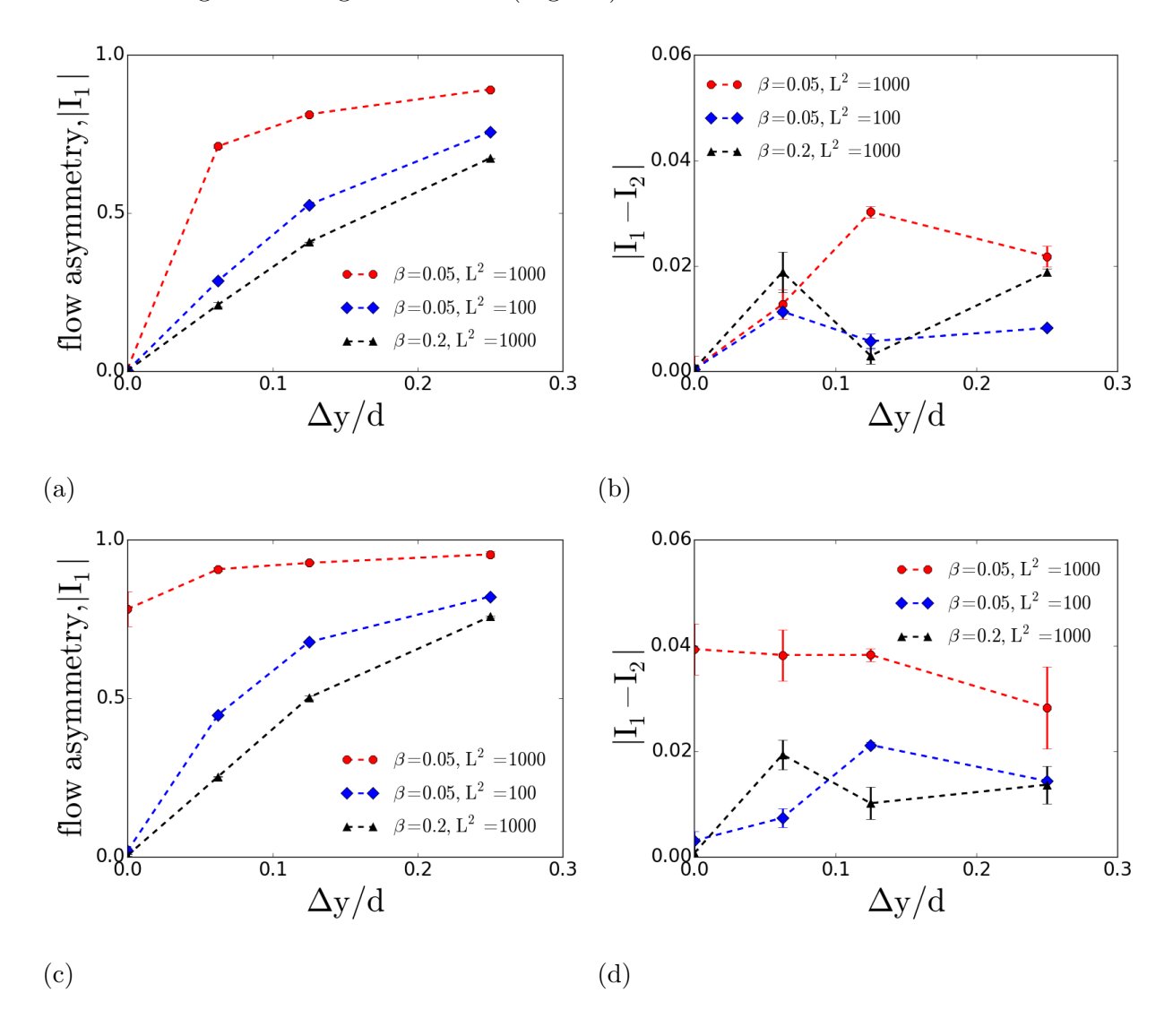


FIG. 11: (a,c) Flow asymmetry around the front cylinder (I_1) and (b,d) the difference between the flow asymmetry around the front and rear cylinders $(I_1 - I_2)$ at (a,b) Wi = 1.88 and (c,d) Wi = 2.5 for different values of Δy and rheological parameters.

Further, we quantify the flow asymmetry around the cylinders in the geometries which have different degrees of geometrical asymmetry (Fig. 11a). Flow asymmetry around the

front cylinder (I_1) increases from $I_1=0$ for symmetric geometry $(\Delta y=0)$ to $I_1\to 1$ as the strength of geometrical asymmetry (Δy) increases. The symmetric flow state at Wi = 1.88 < Wi_{cr2} in the symmetric geometry leads to $I_1 = 0$ at $\Delta y = 0$. Whereas, the viscoelastic interaction between the front and the off-center located rear cylinder leads to $I_1 > 0$ in asymmetric geometries. Strong shear-thinning destabilizes the symmetric flow states in viscoelastic flows [10, 27]. Therefore, the value of I_1 at $\beta = 0.05$ is larger than the value at $\beta = 0.2$. For the range of Δy reported in this study, I_1 increases almost linearly with Δy at $\beta = 0.2$. Whereas due to a stronger shear-thinning effect at $\beta = 0.05$, I_1 increases rapidly with Δy and saturates at a smaller value of Δy (Fig. 11a). The elasticity of the fluid decreases as the value of L^2 decreases, which stabilizes the symmetric flow states [10, 27]. Therefore, the value of I_1 at $L^2 = 100$ is smaller than $L^2 = 1000$ (Fig. 11a). We also calculate $I_1 - I_2$ to quantify the spanwise transport of fluid between the cylinders (Fig. 11b). There is not any spanwise transport of fluid at $\Delta y = 0$, because the flow state is symmetric. In the asymmetric geometries at $\beta = 0.05$, the spanwise transport of fluid between the cylinders initially increases with Δy and after achieving a maximum value it decreases. However, $I_1 - I_2$ does not show any clear trend at $\beta = 0.2$. Despite the different trends, the values of $I_1 - I_2$ are small $(I_1 - I_2 < 0.04)$. At Wi = 2.5 > Wi_{cr2}, the flow becomes asymmetric even in the symmetric geometry for rheological properties $\beta = 0.05$ and $L^2 = 1000$ (Fig. 5a). Therefore, I_1 and $I_1 - I_2$ have nonzero values in the symmetric geometry ($\Delta y = 0$) at Wi = 2.5 (Figs. 11c and 11d). The value of Wi_{cr2} increases as the shear-thinning strength or the elasticity of the fluid decreases [10]. Therefore, the behaviors of I_1 and $I_1 - I_2$ for the fluids with other values of rheological parameters at Wi = 2.5 (Figs. 11c and 11d) are similar to the behaviors at Wi = 1.88 (Figs. 11a and 11b).

IV. CONCLUSIONS

Porous medium is intrinsically disordered and consists of asymmetric pores. Here, we study pore-scale viscoelastic instability in an asymmetric geometry made of two cylinders located inside a channel and explore the effect of geometrical asymmetry and fluid rheological properties on viscoelastic instability-induced flow states. The front cylinder is located on the centerline of the channel, whereas the rear cylinder is off-center, leading to an asymmetric geometry. In asymmetric geometries, the flow around the cylinders is always asymmetric

due to the hydrodynamic interaction between the cylinders, and the strength of flow asymmetry increases with Wi until it saturates. Along with the asymmetric flow around the cylinders at intermediate Wi ($Wi_{cr1} < Wi < Wi_{cr2}$), a single recirculating eddy appears in the region between the cylinders, whose size decreases as the strength of geometrical asymmetry increases. At large Wi ($Wi > Wi_{cr2}$), the eddy between the cylinders disappears, and flow around cylinders becomes completely asymmetric. The size and the stability of the eddy increase as the shear-thinning strength of fluid decreases.

V. ACKNOWLEDGMENTS

A.M.A. acknowledges financial support from the National Science Foundation through Grants No. CBET-1700961 and CBET-2141404.

VI. APPENDIX

A. Entrance and exit effect

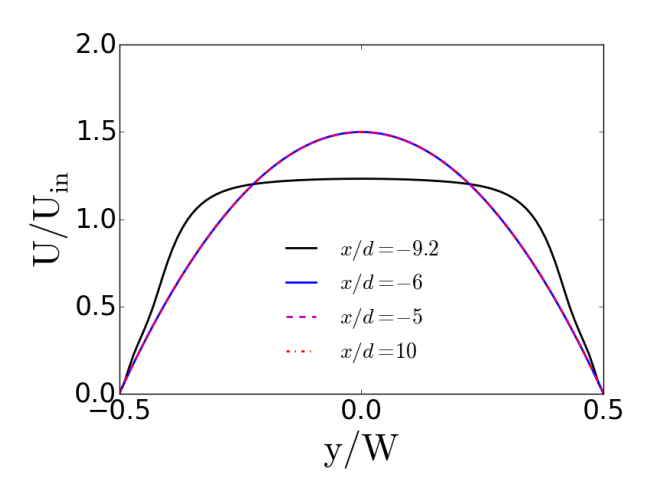


FIG. 12: The velocity profile at different locations along the length of the channel at Wi = 0.62. The entrance and the exit of the channel are at x = -9.4d and x = 15.6d, respectively. The front cylinder is located at x = 0.

The hydrodynamic entrance length for channel flow can be estimated as [57]:

$$L_{entrance} = 0.05 Re_D D, (7)$$

where D is the hydraulic diameter of the channel and $\text{Re}_D = \rho U_{in}D/\mu$ is the Reynolds number based on the hydraulic diameter. In the present study, the value of hydrodynamic entrance length varies from $L_{entrance} = 10^{-4}d$ at Wi = 0.62 to $L_{entrance} = 6 \times 10^{-4}d$ at Wi = 3.75, where d is the cylinder diameter. The locations of the entrance, exit and front cylinder are x/d = -9.4, x/d = 15.6, and x/d = 0, respectively. Thus, the length of the channel in the present study is 25d and the front cylinder is located 9.4d downstream from the inlet, which is much larger than the hydrodynamic entrance length. We have also plotted the velocity profile at different locations along the length of the channel, which clearly shows that the velocity profile sufficiently upstream of the front cylinder becomes fully developed (Fig. 12). The flow also becomes fully developed downstream of the rear cylinder much before the exit (Fig. 12).

B. Mesh and time-step dependence study

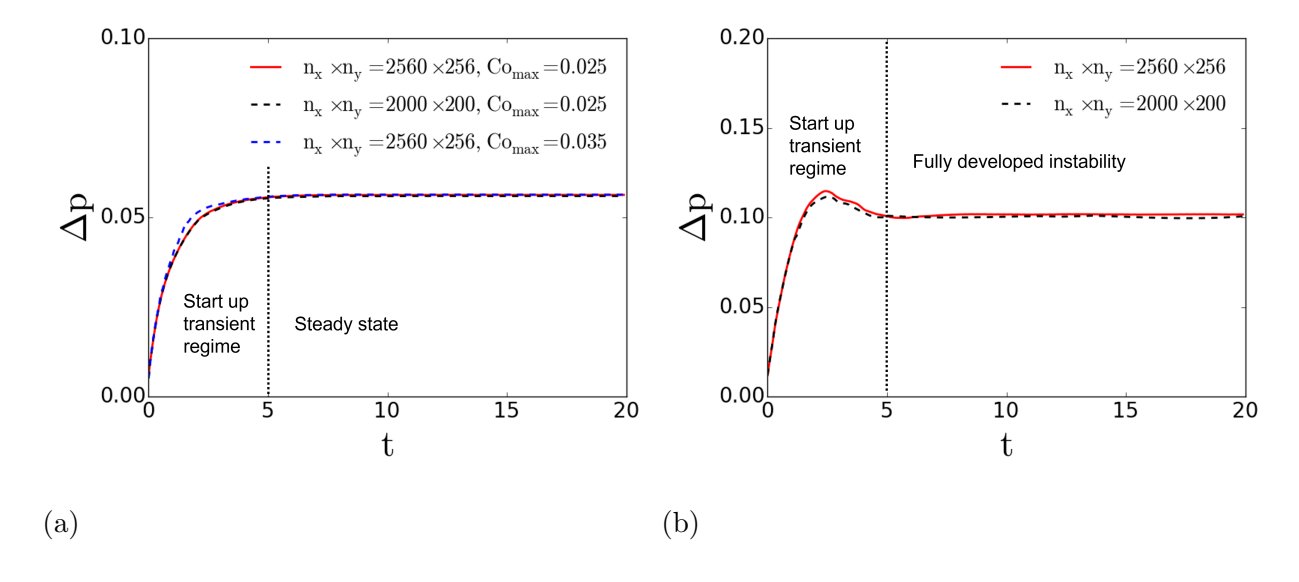


FIG. 13: Normalized pressure drop across the channel at (a) Wi = 0.62 and (b) Wi = 3.75. Other parameters are $\beta = 0.05$ and $L^2 = 1000$.

We use pressure drop (Δp) across the channel as a metric for mesh and time-independent studies [10]. The pressure drop across the channel for different numerical meshes and the different values of the Courant numbers have been shown in Fig. 13a for a small Wi (Wi = 0.62). At a small Wi, the simulation achieves a steady-state for t > 5 and Δp becomes constant. The simulation becomes mesh independent for $n_x \times n_y > 2000 \times 200$, where n_x and n_y are the numbers of grid points along the length and the width of the channel (Fig. 13a). The simulations in the present study have been performed using $n_x \times n_y = 2560 \times 256$. The Courant number (Co) controls the time-step size in the present study and it has been defined as:

$$Co = \tau \Delta t, \tag{8}$$

where Δt is the simulation time-step. τ is a characteristic time scale based on the local cell flow scales and defined as:

$$\tau = \frac{1}{2V} \sum_{faces_i} |\phi_i|,\tag{9}$$

where V and ϕ are cell volume and the cell-face volumetric flux. \sum_{faces_i} shows the summation over all cell faces. The simulation becomes time-step independent for $\text{Co}_{\text{max}} < 0.035$ (Fig. 13a). We use $\text{Co}_{\text{max}} = 0.025$ in the present study. We also check the convergence at the maximum Wi (Wi = 3.75) used in the present study and ensure that the results are mesh independent even at the maximum Wi (Fig. 13b). The instability becomes fully developed for t > 5 and Δp fluctuates around a well-defined mean (Fig. 13b). However, the standard deviation of the fluctuation is very small (< 1% of the mean value). Therefore, the fluctuation is very weak and the flow remains almost steady even at the maximum Wi in the present study.

C. Time dependent flow asymmetry around cylinder

The value of flow asymmetry fluctuates around a well-defined mean once the instability becomes fully developed (Fig. 14). The standard deviation of the fluctuation is 0.24% of the mean value at Wi = 3.75.

D. The Pakdel–McKinley (M) parameter

The Pakdel–McKinley (M) is widely used to characterize the criteria for elastic instability in curved geometry [1, 2]. The Pakdel–McKinley parameter is defined as:

$$M = \left[\frac{\tau_{11}}{\eta_0 \dot{\gamma}} \lambda U \kappa\right]^{1/2},\tag{10}$$

where τ_{11} , $\dot{\gamma}$, and κ are the local tensile stress along the streamline direction, the magnitude of the shear rate, and streamline curvature, respectively. The details to calculate these variables

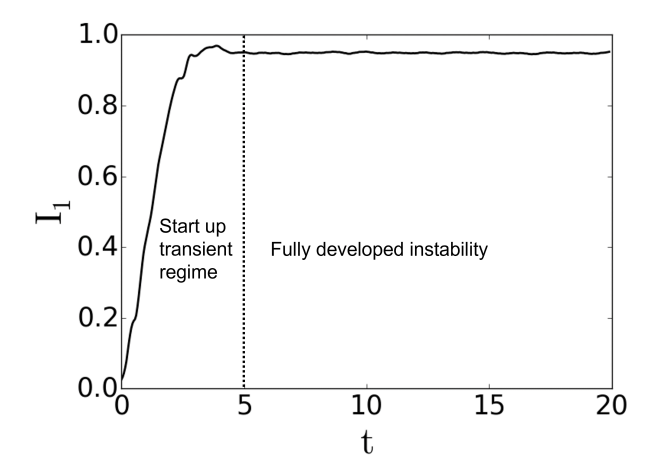


FIG. 14: Flow asymmetry around the front cylinder in the asymmetric geometry $(\Delta y = d/16)$ at Wi = 3.75 for $\beta = 0.05$ and $L^2 = 1000$. The standard deviation of the fluctuation of I_1 in the fully-developed regime is 0.24% of the mean value.

can be found in the literature [10, 38]. The elastic instability occurs when $M \ge M_{\rm crit}$. The spatial profiles of the M parameter in the asymmetric geometry at different Wi (< Wi_{cr1}) have been shown in Fig. 15. The location where the value of M is maximum is the most sensitive region to the instability [10]. Similar to the symmetric geometry [10], the location of $M_{\rm max}$ shifts from the side of the rear cylinder to the region in between the cylinders as Wi \rightarrow Wi_{cr1} (Fig. 15) and hence the formation of new flow state at Wi_{cr1} < Wi < Wi_{cr2} occurs due to instability in the region between the cylinders.

[1] G. H. McKinley, P. Pakdel, and A. Öztekin, Rheological and geometric scaling of purely elastic flow instabilities, Journal of Non-Newtonian Fluid Mechanics 67, 19 (1996).

^[2] P. Pakdel and G. H. McKinley, Elastic instability and curved streamlines, Physical Review Letters 77, 2459 (1996).

^[3] S. Aramideh, P. P. Vlachos, and A. M. Ardekani, Pore-scale statistics of flow and transport through porous media, Physical Review E 98, 1 (2018).

^[4] C. A. Browne, A. Shih, and S. S. Datta, Pore-scale flow characterization of polymer solutions in microfluidic porous media, Small, 1903944 (2019).

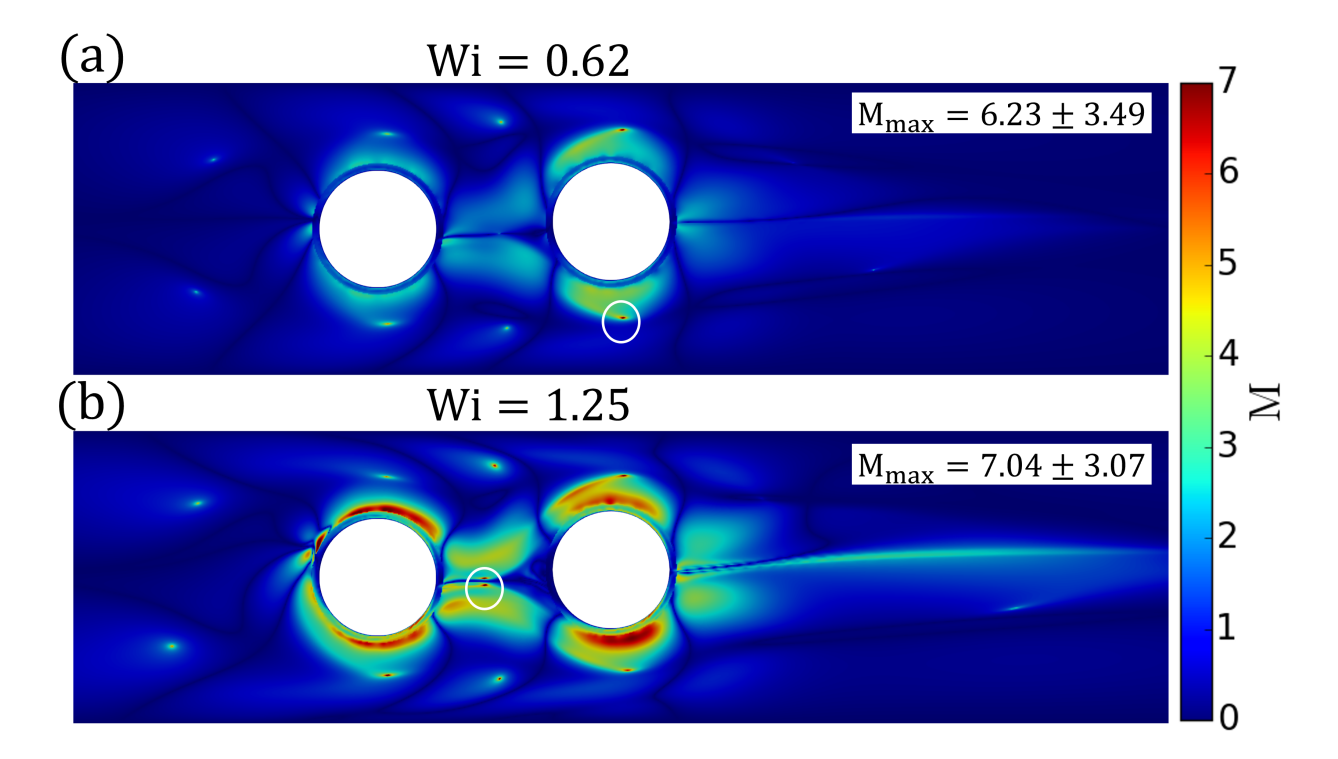


FIG. 15: The Pakdel–McKinley (M) parameter in the asymmetric geometry ($\Delta y = d/16$) at (a) Wi = 0.62 and (b) Wi = 1.25. Other parameters are $\beta = 0.05$, $L^2 = 1000$, and t = 17.5 (steady state). White circles indicate the regions of M_{max} . The values of M_{max} represent the mean and the standard deviation obtained over 3×3 pixel area centered at the point of maximum value of M.

- [5] M. Kumar, J. S. Guasto, and A. M. Ardekani, Transport of complex and active fluids in porous media, Journal of Rheology 66, 375 (2022).
- [6] K. S. Sorbie, Polymer-improved oil recovery (Springer Science & Business Media, 2013).
- [7] D. Roote, Technology status report: in situ flushing, Ground Water Remediation Technology Analysis Center (available at http://www.gwrtac.org) (1998).
- [8] D. Kawale, G. Bouwman, S. Sachdev, P. L. Zitha, M. T. Kreutzer, W. R. Rossen, and P. E. Boukany, Polymer conformation during flow in porous media, Soft matter 13, 8745 (2017).
- [9] M. Kumar, S. Aramideh, C. A. Browne, S. S. Datta, and A. M. Ardekani, Numerical investigation of multistability in the unstable flow of a polymer solution through porous media, Physical Review Fluids 6, 033304 (2021).
- [10] M. Kumar and A. M. Ardekani, Elastic instabilities between two cylinders confined in a channel, Physics of Fluids 33, 074107 (2021).

- [11] D. M. Walkama, N. Waisbord, and J. S. Guasto, Disorder suppresses chaos in viscoelastic flows, Physical Review Letters 124, 164501 (2020).
- [12] K. Weissenberg, A continuum theory of rhelogical phenomena (1947).
- [13] A. Groisman and V. Steinberg, Elastic turbulence in a polymer solution flow, Nature **405**, 53 (2000).
- [14] A. Groisman and V. Steinberg, Efficient mixing at low reynolds numbers using polymer additives, Nature **410**, 905 (2001).
- [15] C. A. Browne and S. S. Datta, Elastic turbulence generates anomalous flow resistance in porous media, Science Advances 7, 10.1126/sciadv.abj2619 (2021).
- [16] S. J. Haward, C. C. Hopkins, and A. Q. Shen, Stagnation points control chaotic fluctuations in viscoelastic porous media flow, Proceedings of the National Academy of Sciences 118, e2111651118 (2021).
- [17] S. De, J. van der Schaaf, N. G. Deen, J. A. M. Kuipers, E. A. J. F. Peters, and J. T. Padding, Lane change in flows through pillared microchannels, Physics of Fluids 29, 113102 (2017).
- [18] S. De, S. P. Koesen, R. V. Maitri, M. Golombok, J. T. Padding, and J. F. M. van Santvoort, Flow of viscoelastic surfactants through porous media, AIChE Journal 64, 773 (2018).
- [19] A. Clarke, A. M. Howe, J. Mitchell, J. Staniland, L. A. Hawkes, et al., How viscoelastic-polymer flooding enhances displacement efficiency, SPE Journal 21, 675 (2016).
- [20] S. De, P. Krishnan, J. van der Schaaf, J. Kuipers, E. Peters, and J. Padding, Viscoelastic effects on residual oil distribution in flows through pillared microchannels, Journal of colloid and interface science 510, 262 (2018).
- [21] P. Stoodley, I. Dodds, D. De Beer, H. L. Scott, and J. D. Boyle, Flowing biofilms as a transport mechanism for biomass through porous media under laminar and turbulent conditions in a laboratory reactor system, Biofouling 21, 161 (2005).
- [22] R. Tang, C. S. Kim, D. J. Solfiell, S. Rana, R. Mout, E. M. Velázquez-Delgado, A. Chompoosor, Y. Jeong, B. Yan, Z. J. Zhu, C. Kim, J. A. Hardy, and V. M. Rotello, Direct delivery of functional proteins and enzymes to the cytosol using nanoparticle-stabilized nanocapsules, ACS Nano 7, 6667 (2013).
- [23] L. Hall-Stoodley, J. W. Costerton, and P. Stoodley, Bacterial biofilms: from the Natural environment to infectious diseases, Nature Reviews Microbiology 2, 95 (2004).

- [24] G. H. McKinley, R. C. Armstrong, and R. A. Brown, The wake instability in viscoelastic flow past confined circular cylinders, Philosophical Transactions of the Royal Society of London. Series A: Physical and Engineering Sciences 344, 265 (1993).
- [25] S. J. Haward, C. C. Hopkins, and A. Q. Shen, Asymmetric flow of polymer solutions around microfluidic cylinders: Interaction between shear-thinning and viscoelasticity, Journal of Non-Newtonian Fluid Mechanics 278, 104250 (2020).
- [26] B. Qin, P. F. Salipante, S. D. Hudson, and P. E. Arratia, Upstream vortex and elastic wave in the viscoelastic flow around a confined cylinder, Journal of Fluid Mechanics 864 (2019).
- [27] S. Varchanis, C. C. Hopkins, A. Q. Shen, J. Tsamopoulos, and S. J. Haward, Asymmetric flows of complex fluids past confined cylinders: A comprehensive numerical study with experimental validation, Physics of Fluids 32, 053103 (2020).
- [28] S. J. Haward, N. Kitajima, K. Toda-Peters, T. Takahashi, and A. Q. Shen, Flow of wormlike micellar solutions around microfluidic cylinders with high aspect ratio and low blockage ratio, Soft Matter 15, 1927 (2019).
- [29] S. Kenney, K. Poper, G. Chapagain, and G. F. Christopher, Large deborah number flows around confined microfluidic cylinders, Rheologica Acta **52**, 485 (2013).
- [30] Y. Zhao, A. Q. Shen, and S. J. Haward, Flow of wormlike micellar solutions around confined microfluidic cylinders, Soft Matter 12, 8666 (2016).
- [31] A. Varshney and V. Steinberg, Elastic wake instabilities in a creeping flow between two obstacles, Physical Review Fluids 2, 051301 (2017).
- [32] X. Shi and G. F. Christopher, Growth of viscoelastic instabilities around linear cylinder arrays, Physics of Fluids 28, 124102 (2016).
- [33] C. A. Browne, A. Shih, and S. S. Datta, Bistability in the unstable flow of polymer solutions through pore constriction arrays, Journal of Fluid Mechanics 890, 10.1017/jfm.2020.122 (2020).
- [34] P. E. Arratia, C. C. Thomas, J. Diorio, and J. P. Gollub, Elastic instabilities of polymer solutions in cross-channel flow, Physical Review Letters **96**, 12 (2006).
- [35] R. J. Poole, M. A. Alves, and P. J. Oliveira, Purely elastic flow asymmetries, Physical Review Letters 99, 1 (2007).
- [36] L. E. Rodd, T. P. Scott, D. V. Boger, J. J. Cooper-White, and G. H. McKinley, The inertioelastic planar entry flow of low-viscosity elastic fluids in micro-fabricated geometries, Journal

- of Non-Newtonian Fluid Mechanics 129, 1 (2005).
- [37] A. Lanzaro and X.-F. Yuan, Effects of contraction ratio on non-linear dynamics of semidilute, highly polydisperse paam solutions in microfluidics, Journal of Non-Newtonian Fluid Mechanics 166, 1064 (2011).
- [38] S. J. Haward, G. H. Mckinley, and A. Q. Shen, Elastic instabilities in planar elongational flow of monodisperse polymer solutions, Scientific Reports 6, 1 (2016).
- [39] M. B. Khan and C. Sasmal, Elastic instabilities and bifurcations in flows of wormlike micellar solutions past single and two vertically aligned microcylinders: Effect of blockage and gap ratios, Physics of Fluids **33**, 033109 (2021).
- [40] M. A. Nilsson, R. Kulkarni, L. Gerberich, R. Hammond, R. Singh, E. Baumhoff, and J. P. Rothstein, Effect of fluid rheology on enhanced oil recovery in a microfluidic sandstone device, Journal of Non-Newtonian Fluid Mechanics 202, 112 (2013).
- [41] S. S. Datta, T. Ramakrishnan, and D. A. Weitz, Mobilization of a trapped non-wetting fluid from a three-dimensional porous medium, Physics of Fluids **26**, 022002 (2014).
- [42] R. B. Bird, P. J. Dotson, and N. L. Johnson, Polymer solution rheology based on a finitely extensible bead-spring chain model, Journal of Non-Newtonian Fluid Mechanics 7, 213 (1980).
- [43] R. Bird, R. Armstrong, and O. Hassager, *Dynamics of polymeric liquids. Vol. 1, 2nd Ed. :*Fluid mechanics (John Wiley and Sons Inc., New York, NY, United States, 1987).
- [44] R. B. Bird, C. F. Curtiss, R. C. Armstrong, and O. Hassager, Dynamics of Polymeric Liquids, Volume 2: Kinetic Theory, 2nd Edition, 2nd ed. (Wiley, 1987).
- [45] M. D. Chilcott and J. M. Rallison, Creeping flow of dilute polymer solutions past cylinders and spheres, Journal of Non-Newtonian Fluid Mechanics 29, 381 (1988).
- [46] P. J. Oliveira, An exact solution for tube and slit flow of a FENE-P fluid, Acta Mechanica 158, 157 (2002).
- [47] H. Jasak, A. Jemcov, and Z. Tukovic, Openfoam: A c++ library for complex physics simulations, International Workshop on Coupled Methods in Numerical Dynamics, 1 (2007), cited By :275.
- [48] F. Pimenta and M. A. Alves, Stabilization of an open-source finite-volume solver for viscoelastic fluid flows, Journal of Non-Newtonian Fluid Mechanics 239, 85 (2017).
- [49] F. Habla, M. W. Tan, J. Haßlberger, and O. Hinrichsen, Numerical simulation of the viscoelastic flow in a three-dimensional lid-driven cavity using the log-conformation reformulation in

- OpenFOAM®, Journal of Non-Newtonian Fluid Mechanics 212, 47 (2014).
- [50] K. Walters and M. F. Webster, The distinctive CFD challenges of computational rheology, International Journal for Numerical Methods in Fluids 43, 577 (2003).
- [51] R. Fattal and R. Kupferman, Constitutive laws for the matrix-logarithm of the conformation tensor, Journal of Non-Newtonian Fluid Mechanics **123**, 281 (2004).
- [52] R. Fattal and R. Kupferman, Time-dependent simulation of viscoelastic flows at high Weissenberg number using the log-conformation representation, Journal of Non-Newtonian Fluid Mechanics 126, 23 (2005).
- [53] B. Qin and P. E. Arratia, Characterizing elastic turbulence in channel flows at low reynolds number, Physical Review Fluids 2, 083302 (2017).
- [54] S. Aramideh, P. P. Vlachos, and A. M. Ardekani, Nanoparticle dispersion in porous media in viscoelastic polymer solutions, Journal of Non-Newtonian Fluid Mechanics **268**, 75 (2019).
- [55] S. De, J. Kuipers, E. Peters, and J. Padding, Viscoelastic flow simulations in model porous media, Physical Review Fluids 2, 053303 (2017).
- [56] B. Purnode and M. J. Crochet, Polymer solution characterization with the FENE-P model, Journal of Non-Newtonian Fluid Mechanics 77, 1 (1998).
- [57] T. L. Bergman, F. P. Incropera, D. P. DeWitt, and A. S. Lavine, Fundamentals of heat and mass transfer (John Wiley & Sons, 2011).